

Robust State Estimation and Integrity Monitoring within Multi-Sensor Navigation System

Shuchen Liu^{*1}, Kaizheng Wang¹, Dirk Abel¹ and René Zweigl¹

Abstract—In autonomous applications, global navigation satellite systems (GNSS) aided inertial navigation system (INS) utilizing an extended Kalman filter (EKF) is the most widely investigated solution for high-rate and high-accurate vehicle states estimation. However, such navigation system suffers from poor parameterization, environment disturbances, human error, or even software and hardware failures under worst-case scenarios. In this paper, a novel scheme of multi-sensor navigation system is proposed, contributing to following research questions: 1) How to provide a reliable state estimation under minor system aberrations, i.e. improve the robustness of navigation system against e.g. inappropriate parameterization or environment disturbances; 2) How to provide system integrity against worst-case scenarios, i.e. significant system aberrations or even failures. The proposed scheme involves extended H_{∞} filter (EHF) for robustness enhancement, zonotope for protection level (PL) generation of the navigation solution and vehicle dynamic model aided fault detection (FD) of the inertial sensor. The designed approach is validated using the recorded data from an experimental platform called 'IRT-Buggy', which is an electrical land vehicle. The results show that the proposed scheme provides reliable integrity monitoring and accurate state estimation, under both real-world and artificial abnormalities and shows significant advantages against conventional 'GNSS+INS+EKF' approach.

Keywords: navigation system, robust state estimation, integrity monitoring, H_{∞} filtering, zonotope, fault detection

I. INTRODUCTION

Recently, considerable efforts have been invested in the field of autonomous driving, due to its huge potentiality in safety and efficiency. For real-time autonomous applications, the navigation system is essential and required to estimate the vehicle states with high accuracy and at high rate. For this purpose, the integration of GNSS and INS via tightly-coupled sensor fusion has been widely studied and applied, combining the strength of both GNSS and INS [1]. Further, robustness and integrity should also be considered as essential requirements for navigation systems in safety-critical applications [2]. The current publication mainly concentrates on following tasks:

- 1) providing a robust navigation estimation against e.g. false parameterization or poor initialization;
- 2) providing an integrity system against worst-case scenarios i.e. sensor failures, including:
 - a) detection and mitigation of sensor failures;
 - b) solution protection i.e. determination of whether the navigation solution is safe to use;
 - c) fallback option, functioning without using the abnormal sensor measurements under failures.

where task a) and b) are the main tasks for integrity systems summarized by [3]. Further, to accomplish the fault detection and exclusion (FDE) process of sensor faults, the integrity system is also required to provide functionality c).

In recent years, the tightly-coupled navigation system implemented with a conventional EKF can provide an accurate navigation solution at high rate and is applied in various applications [1]. However, the EKF cannot guarantee a reliable vehicle states estimation in cases of lousy state initialization or inexact noise statistics. [4] states that an alternative EHF can outperform the EKF in terms of against the system uncertainties. However, the application of an EHF for the tightly-coupled GNSS aided INS and its robustness against real-world uncertainties remains to be studied.

To realize FDE of GNSS aided INS, the previous works [5] and [6] has proposed a strategy based on receiver autonomous integrity monitoring (RAIM) and robust set inversion via interval analysis (RSIVIA) against faulty GNSS measurements. Based on [5] and [6], it is assumed in current publication, that a set of fault-free GNSS measurements is fed into the navigation system. Therefore, the current work concentrates on filter-based FDE for the other integrated sensor, i.e. inertial measurement unit (IMU).

To achieve filter-based FD within GNSS aided INS, various researches have been carried out. [7] presents an FD method based on H_{∞} filtering, designed for a loosely-coupled GNSS aided INS. In [7] not only the accelerometer and gyroscope bias are modeled, but also their unexpected faults. This results in a relatively high system order and huge computational load. [8] proposes a sequential Kalman filter (KF)-based integrity monitoring for tightly-coupled navigation system. However, [8] concentrates on FD of GNSS measurements. Further, in [7] and [8], FD is realized by comparing an innovation-based test statistic with its threshold, which is generated by statistic analysis and, therefore, is statistically sensitive. This drawback might be compensated by introducing additional information into the threshold generation, e.g. control system inputs and vehicle dynamic model, which is studied in the present work.

For solution protection of the navigation system, a guaranteed PL is strongly demanded, which bounds the estimation error satisfying the predefined integrity risk. PL can be generated by applying statistic approaches, which calculate the confidence interval assuming that statistical distribution of the estimation error is known [9]. However, the assumption about the estimation error distribution might be difficult to validate [10]. Under such consideration, set-membership approaches might be a promising alternative for statistic ap-

¹Institute of Automatic Control, RWTH Aachen University, Germany.

*corresponding author, email: s.liu@irt.rwth-aachen.de

proaches. Set-membership approaches rely on the description of uncertainties by known compact sets and estimate the system states as a compact set enclosing all the sets of states that are consistent with process and measurement uncertainties [11]. Interval arithmetic can be used to generate guaranteed bounds by utilizing interval extensions [12]. The drawback of this approach is the severe overestimation due to interval dependency and the wrapping effect [13]. As an alternative set representation, zonotope is shown to be suitable to control the wrapping effect [10]. In [14], zonotope combined with an estimation observer, is capable of providing robust interval calculation of estimation error for descriptor systems, proved in simulation environment. The performance of applying zonotope on high-order nonlinear system, i.e. tightly-coupled navigation system, remains to be researched.

In the present publication, a novel scheme illustrated in Fig. 1 is applied within a tightly-coupled GNSS aided INS, aiming at providing a navigation solution with high accuracy, robustness and integrity. Under nominal operation, the fault-free GNSS observables, i.e. pseudoranges and deltaranges, and IMU measurements are fused within an EHF (main filter). FD of IMU failures is realized by comparing the estimated vehicle dynamic with its generated threshold. The vehicle dynamic, specifically the measurements of acceleration in x-direction and rotational rate in z-direction, is calculated using IMU measurements and estimated IMU bias from the main filter. Meanwhile, the thresholds are generated with the aided information from the relatively low-precision vehicle dynamic model. The threshold generation does not rely on probability calculations or fault models, and therefore, is effective to detect various sorts of IMU measurement faults without being statistically sensitive. Under IMU failure, the fallback filter, which does not utilize faulty IMU measurements, is activated to ensure the integrity and continuity of the navigation solution. Further, zonotope is applied to generate PL for the estimated states by both main and fallback filter.

The designed approach is evaluated in post-processing environment using the recorded data, utilizing an experimental platform 'IRT-Buggy' [15]. In order to reproduce

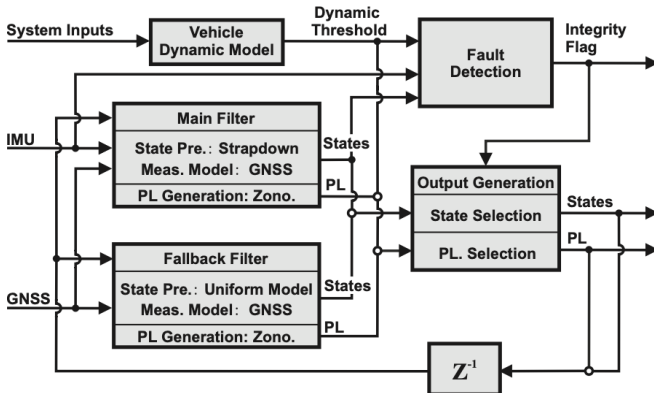


Fig. 1. General overview of the navigation and integrity system

the test scenario, measurements of all involved sensors, the control signals of the vehicle and GNSS correction data are recorded. In the experimental evaluation, EHF is compared with EKF under inappropriate filter parameterization and poor initialization, regarding the position estimation accuracy. Further, the PL generation using zonotope is validated by checking the consistency of the estimated error bound with real-time-kinematic (RTK) ground truth. Finally, the dynamic model aided FD is validated under real-world and artificial IMU failures, while the performance of the fallback filter is evaluated in this scenario.

The rest of this paper is structured as follows: In Sec. II, the basic theory of H_∞ filtering and zonotope is introduced, followed by their realization and integration into the existing tightly-coupled navigation system. Further, the dynamic model aided FD is introduced, including the threshold generation of vehicle dynamic using interval operation. In Sec. III, the measurement setup and target hardware are described, followed by the parameterization, experimental results are evaluated and discussed afterwards. Finally, Sec. IV draws the conclusion of the current work, analyses the feasibility of applying the designed approach into various application domains, and provides an outlook for future developments.

II. METHODOLOGY

A. Theory of Extended H_∞ Filter

In this section, the basics of EHF are introduced, considering a nonlinear time discrete system given as follows:

$$\mathbf{x}_{k+1} = \mathbf{f}(\mathbf{x}_k) + \mathbf{G}_k \mathbf{w}_k, \quad \mathbf{w}_k \sim \mathcal{N}(0, \mathbf{Q}_k), \quad (1)$$

$$\mathbf{z}_k = \mathbf{h}(\mathbf{x}_k) + \mathbf{\nu}_k, \quad \mathbf{\nu}_k \sim \mathcal{N}(0, \mathbf{R}_k), \quad (2)$$

$$\mathbf{y}_k = \mathbf{L}_k \mathbf{x}_k, \quad (3)$$

where \mathbf{x}_{k+1} and \mathbf{x}_k are the states vector for time instance $k+1$ and k , respectively. \mathbf{z}_k is the measurement vector. \mathbf{f} and \mathbf{h} are the nonlinear time-invariant state transition and measurement functions, respectively. \mathbf{w}_k and $\mathbf{\nu}_k$ are process and measurement noise, respectively. \mathbf{G}_k donates the shaping matrix, which maps the process noise \mathbf{w}_k into the state vector. In H_∞ filtering theory, \mathbf{w}_k and $\mathbf{\nu}_k$ are not required to satisfy white Gaussian distribution. Instead, the noise distribution could be nonzero mean, deterministic or even unknown statistics [4]. In order to compare the performance of EHF with EKF, \mathbf{w}_k and $\mathbf{\nu}_k$ are still assumed to satisfy white Gaussian distribution in this work, whose variance matrices are \mathbf{Q}_k and \mathbf{R}_k , respectively. For poorly parameterized \mathbf{Q}_k and \mathbf{R}_k , the performance of the EHF is expected to be less affected than the conventional EKF, showing the robustness of EHF [16]. \mathbf{y}_k denotes the deserved estimated vector at time instance k , which is a linear combination of state vector achieved by user-defined matrix \mathbf{L}_k . With respect to navigation solution, all states in \mathbf{x}_k shall be weighted identical, such that \mathbf{L}_k is defined as unit matrix \mathbf{I} in the current work. The complete H_∞ filtering computation is rigorously deactivated in [4] and summarized

in [17] as:

$$\hat{x}_k^- = \mathbf{f}(\hat{x}_{k-1}^+), \quad (4)$$

$$\hat{P}_k^- = \mathbf{F}_{k-1} \hat{P}_{k-1}^+ \mathbf{F}_{k-1}^T + \mathbf{G}_{k-1} \mathbf{Q}_{k-1} \mathbf{G}_{k-1}^T, \quad (5)$$

$$\hat{P}_k^+ = \hat{P}_k^- \left[\mathbf{I} - \gamma^{-1} \mathbf{L}_k^T \mathbf{L}_k \hat{P}_k^- + \mathbf{H}_k^T \mathbf{R}_k^{-1} \mathbf{H}_k \hat{P}_k^- \right], \quad (6)$$

$$\mathbf{K}_k = \hat{P}_k^+ \mathbf{H}_k^T \mathbf{R}_k^{-1}, \quad (7)$$

$$\hat{x}_k^+ = \hat{x}_k^- + \mathbf{K}_k (\mathbf{z}_k - \mathbf{h}(\hat{x}_k^-)), \quad (8)$$

where \hat{x}_k^- , \hat{x}_k^+ , \hat{P}_k^- and \hat{P}_k^+ denote the a-priori and a-posteriori state and covariance estimate, respectively. \mathbf{F}_{k-1} and \mathbf{H}_{k-1} are the Jacobian matrix of \mathbf{f} and \mathbf{h} , linearized at the operating points, respectively. \mathbf{K}_k is the filter gain matrix. It should be noted that the calculation of \mathbf{K}_k involves a parameter γ , which is discussed in the rest of this section.

The purpose of the optimal H_∞ filtering is to choose the suitable estimation strategies that minimizes a cost function:

$$J = \frac{\sum_{k=0}^{N-1} \|\mathbf{x}_k - \hat{\mathbf{x}}_k^+\|_{\mathbf{L}_k^T \mathbf{L}_k}^2}{\|\mathbf{x}_0 - \hat{\mathbf{x}}_0\|_{\mathbf{P}_0^{-1}}^2 + \sum_{k=0}^{N-1} (\|\mathbf{w}_k\|_{\mathbf{Q}_k^{-1}}^2 + \|\boldsymbol{\nu}_k\|_{\mathbf{R}_k^{-1}}^2)}, \quad (9)$$

where \mathbf{x}_0 , $\hat{\mathbf{x}}_0$ and \mathbf{P}_0 represent initial state vector, its estimation and the covariance of the initialization error, respectively. N denotes the current epoch. The cost function J can be understood as a normalization of all the historical estimation error of \mathbf{y}_k from epoch 0 to the last epoch $N-1$, relative to initialization error $\mathbf{x}_0 - \hat{\mathbf{x}}_0$, process noise \mathbf{w}_k and measurement noise $\boldsymbol{\nu}_k$. The choice of the cost function J is based on game theory approach and assumed to improve the filter robustness against worst-case scenarios [4].

However, the cost function can not be directly minimized [4]. Thus, a performance bound γ is introduced as a constraint for the optimization problem:

$$J < \gamma. \quad (10)$$

Solving the constrained optimization problem results in the the estimation strategy given in Eq. (6) ~ (8). Meanwhile, the constrained optimization problem is only solvable, when the following inequality condition is satisfied for all epoch $k \in \{1, \dots, N\}$ [4]:

$$(\hat{P}_k^-)^{-1} + \mathbf{H}_k^T \mathbf{R}_k^{-1} \mathbf{H}_k - \gamma^{-1} \mathbf{L}_k^T \mathbf{L}_k \succ 0. \quad (11)$$

where ' \succ ' donates that the resulting matrix on the left hand side is positive-definite. It can be observed that, the smaller is γ , the more difficult that Eq. (11) can be satisfied. Thus, γ shall not be chosen too small. The choice γ in the vicinity of zero might cause the divergence of the EHF [18]. On the other hand, [4] describes γ as a measure of filter robustness, i.e. the smaller γ , the smaller estimation error in worst-case scenarios, and therefore, the stronger robustness of the filter. Therefore, the choice of γ is crucial and decides the EHF performance. In practice, γ could be either chosen conservatively by experience, or be estimated by solving the linear matrix inequality (LMI) problem described by Eq. (11). In the current work, an LMI solver from MATLAB® is utilized to calculate γ .

B. Design of Main and Fallback Filter

The EHF is embedded into an existing GNSS/INS navigation system, which is introduced in the previous work [1]. Fig.2 illustrates the state transition within the main filter. Sensor data is pre-processed before being fused in the EHF. Additionally, an integrity monitoring is performed after the GNSS observables are pre-processed, such that a set of fault-free GNSS measurements is fed into the EHF. Only slight changes are required to adjust this structure to the fallback filter, where IMU measurements are not applied: the state prediction with strapdown (gray block) shall be replaced with a uniform velocity model; the state vector shall be adjusted. These will be explained in the following part of this section.

State Vector: In the main filter, the state vector \mathbf{x} is defined as:

$$\mathbf{x} = (\mathbf{p}_{eA}^{e,T} \mathbf{v}_{eA}^{n,T} \mathbf{q}_b^n \mathbf{b}_a^T \mathbf{b}_g^T \mathbf{c}_b \mathbf{c}_d)^T, \quad (12)$$

where 'A' stands for antenna body-frame, 'b' for IMU body-frame, 'e' for earth-centered-earth-fixed (ECEF) coordinates and 'n' for navigation frame. $\mathbf{p}_{eA}^e \in \mathbb{R}^{3 \times 1}$ represents the position of antenna body-frame origin in ECEF frame. $\mathbf{v}_{eA}^n \in \mathbb{R}^{3 \times 1}$ is the velocity of antenna body-frame origin with respect to ECEF frame, expressed in navigation frame north-east-down (NED) coordinates. A quaternion $\mathbf{q}_b^n \in \mathbb{R}^{4 \times 1}$ for the alignment of IMU body frame and navigation frame is estimated, as the expression of vehicle attitude. Additionally, accelerometer bias \mathbf{b}_a and gyroscope bias \mathbf{b}_g , each of dimension $\mathbb{R}^{3 \times 1}$, are part of the state vector, which are necessary for integrating IMU measurements. Further, the receiver clock bias \mathbf{c}_b and drift \mathbf{c}_d are estimated, which are essential for tightly-coupled GNSS integration.

In the fallback filter, the state vector \mathbf{x}_f ('f' stands for fallback) is defined as:

$$\mathbf{x}_f = (\mathbf{p}_{eA}^{e,T} \mathbf{v}_{eA}^{n,T} \mathbf{c}_b \mathbf{c}_d)^T. \quad (13)$$

Without applying IMU measurement in this filter, the IMU relevant biases are removed from the state vector, as well as the vehicle attitude, because the accurate attitude estimation would not be possible without the gyroscope measurements.

Process Model: In the main filter, the system states are propagated by a time-continuous strapdown algorithm shown in Fig.2. The algorithm uses the measurements of IMU accelerometer and gyroscope as inputs and is introduced in

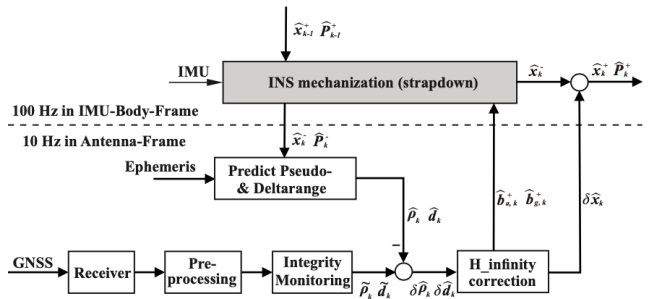


Fig. 2. State transition in the main filter

[1]. Besides, the propagation of the IMU biases is assumed as a first-order Gauss-Markov process [19]. The derivation and calculation of \mathbf{F}_k and \mathbf{G}_k are given in [3] and [20].

In the fallback filter, a so-called uniform model, which assumes that the acceleration and rotational rate of the vehicle are zero and the position change is the integration of the velocity, is applied to replace the strapdown algorithm. Besides, \mathbf{F}_k and \mathbf{G}_k in Eq.(5) are derived from the uniform model.

Measurement Model: The integration of a measurement is achieved by utilizing a measurement equation given in Eq.(2). Specifically, the measurement model in the main filter is composed of the transition from the states to the GNSS observables, i.e. pseudoranges and deltaranges.

The pseudoranges measurement equation is given as:

$$\tilde{\rho} = \|\mathbf{p}_{es}^e - \mathbf{p}_{eA}^e\| + c_b + c_s + I_r + T_r + M_\rho + \nu_\rho, \quad (14)$$

where $\tilde{\rho}$ is the measured scalar pseudorange, \mathbf{p}_{es}^e and \mathbf{p}_{eA}^e represent the position of a satellite (denoted by 's') and the antenna with respect to ECEF coordinates displayed in ECEF, respectively. The terms c_b , c_s , I_r , T_r , M_ρ and ν_ρ in Eq.(14) represent the receiver clock and satellite errors, the ionospheric error, the tropospheric error, multi-path error, and additive measurement noise, respectively. The correction of the error sources is given in [1].

The deltaranges observation is calculated as:

$$\tilde{d} = (\mathbf{e}_{As}^n)^T (\mathbf{v}_{es}^n - \mathbf{v}_{eA}^n) + c_d + \nu_d, \quad (15)$$

where \tilde{d} is the measured scalar relative velocity between antenna and satellite, known as deltaranges. The vector \mathbf{e}_{As}^n is the direction from the antenna to a satellite. The terms \mathbf{v}_{es}^n and \mathbf{v}_{eA}^n represent the velocity of the satellite and antenna with respect to navigation frame, respectively. The terms c_d and ν_d represent the clock drift and the random noise in measurement, respectively.

In practice, the GNSS observables are measured in antenna body-frame, while the strapdown algorithm propagates the system state vector in IMU body-frame, shown in Fig. 2. In the main filter, this requires a transformation from the defined vehicle states \mathbf{p}_{eA}^e and \mathbf{v}_{eA}^n to the required states in IMU body-frame \mathbf{p}_{eb}^e and \mathbf{v}_{eb}^n , shown as:

$$\mathbf{p}_{eb}^e = \mathbf{p}_{eA}^e - \mathbf{C}_n^e \mathbf{C}_b^n \mathbf{L}_A^b, \quad (16)$$

$$\mathbf{v}_{eb}^n = \mathbf{v}_{eA}^n - \mathbf{C}_b^n (\boldsymbol{\omega}_{eb}^b \times \mathbf{L}_A^b), \quad (17)$$

where \mathbf{C}_e^n and \mathbf{C}_b^n denotes the direction cosine matrix for vector rotation among coordinate frames, derived from the estimated antenna position \mathbf{p}_{eA}^e and estimated attitude \mathbf{q}_b^n , respectively. The transformation uses the level arm of the antenna position in IMU body-frame \mathbf{L}_A^b , measured and given in Sec. III-A, and considers the translation velocity of the antenna caused by its rotation $\boldsymbol{\omega}_{eb}^b$, derived from the IMU measurement and estimated IMU bias \mathbf{b}_g [20]. Meanwhile, such transformation is not necessary in the fallback filter, because \mathbf{p}_{eA}^e and \mathbf{v}_{eA}^n are directly part of the state vector.

Eq. (14) and (15) give the measurement equations of a single satellite and are applied to all observed satellites within

both main filter and fallback filter as a measurement update step. Rigorous calculations and derivations, e.g. linearization and calculation of \mathbf{H}_k , are given in [1], [3] and [20].

C. Theory of Zonotope

The PL of navigation states defined in Eq. (12) and (13) are computed using the zonotope. In this section, the definition and necessary background knowledge of zonotope are introduced briefly.

Definition 1. Zonotope is a special class of convex polytope. An n -dimensional zonotope with m -order $\mathbb{Z} \subset \mathbb{R}^n$ ($n \leq m$) is an affine transformation of a hypercube $\mathbb{B}^m = [-1, 1]^m$ as follows [14]:

$$\mathbb{Z} = \{\mathbf{a} \in \mathbb{R}^n | \mathbf{a} = \mathbf{c} + \mathbf{H}\mathbf{b}, \forall \mathbf{b} \in \mathbb{B}^m\}, \quad (18)$$

where vector $\mathbf{c} \in \mathbb{R}^n$ is the center of \mathbb{Z} . $\mathbf{H} \in \mathbb{R}^{n \times m}$ is called the generation matrix of zonotope \mathbb{Z} , which defines the shape and direction of \mathbb{Z} . Each column of $\mathbf{H} = [\mathbf{h}_1, \dots, \mathbf{h}_m]$ donates a translation direction and amplitude in Euclidean space. For a simple expression, $\mathbb{Z} = \langle \mathbf{c}, \mathbf{H} \rangle$ is used in the current work to denote a zonotope.

Property 1.1. The Minkowski sum of two zonotopes $\mathbb{Z}_1 = \langle \mathbf{c}_1, \mathbf{H}_1 \rangle \subset \mathbb{R}^n$ and $\mathbb{Z}_2 = \langle \mathbf{c}_2, \mathbf{H}_2 \rangle \subset \mathbb{R}^n$ is also a zonotope, which can be computed as:

$$\langle \mathbf{c}_1, \mathbf{H}_1 \rangle \oplus \langle \mathbf{c}_2, \mathbf{H}_2 \rangle = \langle \mathbf{c}_1 + \mathbf{c}_2, [\mathbf{H}_1 \ \mathbf{H}_2] \rangle, \quad (19)$$

where \oplus denotes the Minkowski sum operator and the operation $[\mathbf{H}_1 \ \mathbf{H}_2]$ denotes the concatenation of matrices.

Property 1.2. The image of a zonotope by a linear transformation \mathcal{L} can be computed by:

$$\mathcal{L} \odot \langle \mathbf{c}, \mathbf{H} \rangle = \langle \mathcal{L}\mathbf{c}, \mathcal{L}\mathbf{H} \rangle, \quad (20)$$

where \odot denotes the linear image operator.

Definition 2. The interval hull box $[\mathbf{a}]$ of a zonotope \mathbb{Z} is the smallest centered interval vector containing \mathbb{Z} [14]. An example of 2-dimensional zonotope with 6-order and its interval hull are depicted in Fig.3. For an m -order zonotope $\mathbb{Z} = \langle \mathbf{c}, \mathbf{H} \rangle \subset \mathbb{R}^n$, its interval hull Box $[\mathbf{a}]$ is computed as follows:

$$[\mathbf{a}_i] = \left[c_i - \sum_{j=1}^m |\mathbf{H}_{ij}|, c_i + \sum_{j=1}^m |\mathbf{H}_{ij}| \right], i \in \{1, \dots, n\}. \quad (21)$$

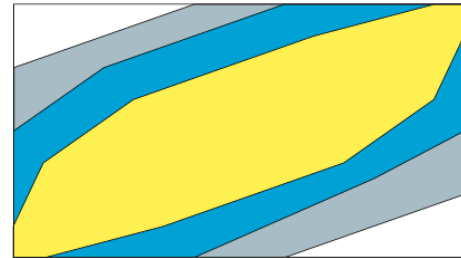


Fig. 3. A zonotope \mathbb{Z} (yellow area), its two-order reduced zonotopes \mathbb{Z}_1 (yellow and blue area), its 3-order reduced zonotope \mathbb{Z}_2 (yellow, blue and gray area) and its interval hull box $[\mathbf{a}]$ (yellow, blue, gray and white area)

Remark 1. When the outer approximation of a zonotope \mathbb{Z} by an aligned box is too conservative, a reduction operator $\mathcal{R}(\mathcal{H})$ can be used to reduce the complexity of \mathbb{Z} [21]. The original zonotope is a subset of the resulting reduced zonotope,

$$\langle \mathbf{c}, \mathcal{H} \rangle \subseteq \langle \mathbf{c}, \mathcal{R}(\mathcal{H}) \rangle, \quad (22)$$

without changing the interval hull box. The reduction order q ($n \leq q \leq m$) shall be defined, specifying the order of the resulting zonotope $\langle \mathbf{c}, \mathcal{R}(\mathcal{H}) \rangle$, where $\mathcal{R}(\mathcal{H}) \in \mathbb{R}^{n \times q}$. The realization of zonotope reduction is given in [14].

In Fig. 3, an example of reducing the 2-dimensional zonotope ($\mathbb{Z} = \langle \mathbf{c}, \mathcal{H} \rangle \subset \mathbb{R}^2$) with 6-order ($\mathcal{H} \in \mathbb{R}^{2 \times 6}$) is illustrated. \mathbb{Z} is reduced to \mathbb{Z}_1 and \mathbb{Z}_2 with reduction order $q_1 = 4$ and $q_2 = 3$, respectively. The smaller reduction order q results in larger overestimation and reduces the computational load. [10] states that the reduction order q is allowed to be freely chosen, compromising between exactness (with larger q) and domain complexity (with smaller q) of the resulting zonotope.

D. PL Generation using Zonotope

The core issue of PL calculation is to bound the state estimation error \mathbf{e}_k . Analog to filter state transition, the estimation of the state error bound $[\mathbf{e}_k]$ also contains a-priori propagation and a-posteriori correction. The error dynamic of EHF is given as follows:

$$\mathbf{e}_k^- = \mathbf{x}_k - \hat{\mathbf{x}}_k^- = \mathbf{F}_{k-1} \mathbf{e}_{k-1}^+ + \mathbf{G}_k \mathbf{w}_{k-1}, \quad (23)$$

$$\mathbf{e}_k^+ = \mathbf{x}_k - \hat{\mathbf{x}}_k^+ = (\mathbf{I} - \mathbf{K}_k \mathbf{H}_k) \mathbf{e}_k^- - \mathbf{K}_k \mathbf{v}_k, \quad (24)$$

where \mathbf{e}_k^- and \mathbf{e}_k^+ represent the a-priori and a-posterior estimation error, respectively. The matrices multiplication and matrices addition in error dynamic model corresponds to linear image \odot and Minkowski sum \oplus in zonotope calculation, respectively.

Assume that the initial estimation error \mathbf{e}_0 , process noise \mathbf{w}_k and measurement noise \mathbf{v}_k are zero-mean and bounded by corresponding zonotopes:

$$\mathbf{e}_0 \in \langle \mathbf{0}, \mathcal{E}_0 \rangle, \mathbf{w}_k \in \langle \mathbf{0}, \mathcal{W}_k \rangle, \mathbf{v}_k \in \langle \mathbf{0}, \mathcal{V}_k \rangle, \quad (25)$$

where \mathcal{E}_0 , \mathcal{W}_k and \mathcal{V}_k represent the generation matrix of corresponding zonotopes. \mathcal{E}_0 shall be initialized large enough, considering the large system uncertainties on the filter initialization stage. \mathcal{W}_k and \mathcal{V}_k are calculated as diagonal matrices with their diagonal elements equal to $n_{\sigma,z}$ times standard deviation of process noise $\sigma_{\mathbf{w}_k}$ and measurement noise $\sigma_{\mathbf{v}_k}$, respectively. $n_{\sigma,z}$ is a pre-defined parameter, corresponding to the confidential level of the resulting zonotope. It should be noted that the calculation of \mathcal{W}_k and \mathcal{V}_k still depends on the statistical distribution of the process and measurement noise in the current work, which is zero-mean normal distribution. However, such distribution is not required by the implementing zonotope. Instead, only the lower and upper bound are required by the zonotope, which can be obtained from the sensor characteristics from the manufacturer or vehicle dynamic limitations. In general, the measurement boundaries are more convenient to obtain

Algorithm 1 EHF Extended with Zonotope

Initialization:

EHF: \mathbf{x}_0 , \mathbf{P}_0 ; Zonotope: \mathcal{E}_0

Propagation:

$$\begin{aligned} \text{EHF: } \hat{\mathbf{x}}_{k-1} &\rightarrow \hat{\mathbf{x}}_k^-, \hat{\mathbf{P}}_{k-1} \rightarrow \hat{\mathbf{P}}_k^- \\ \text{Zonotope: } \mathcal{E}_{k-1} &\rightarrow \mathcal{E}_k^- \end{aligned} \quad \begin{aligned} \text{Eq. (4) (5)} \\ \text{Eq. (28)} \end{aligned}$$

Measurement Update:

$$\begin{aligned} \text{if new measurements available then} \\ \text{EHF: } \hat{\mathbf{P}}_k^- \rightarrow \hat{\mathbf{P}}_k^+, \hat{\mathbf{x}}_k^- \rightarrow \hat{\mathbf{x}}_k^+ \\ \text{Zonotope: } \mathcal{E}_k^- \rightarrow \mathcal{E}_k^+ \\ \text{end if} \end{aligned} \quad \begin{aligned} \text{Eq. (6) (7) (8)} \\ \text{Eq. (29)} \end{aligned}$$

Output Generation:

$$\begin{aligned} \text{if new measurements available then} \\ \hat{\mathbf{P}}_k = \hat{\mathbf{P}}_k^+, \hat{\mathbf{x}}_k = \hat{\mathbf{x}}_k^+, \mathcal{E}_k = \mathcal{E}_k^+ \\ \text{else} \\ \hat{\mathbf{P}}_k = \hat{\mathbf{P}}_k^-, \hat{\mathbf{x}}_k = \hat{\mathbf{x}}_k^-, \mathcal{E}_k = \mathcal{E}_k^- \\ \text{end if} \\ \mathcal{E}_k \rightarrow [\mathbf{e}_k] \end{aligned} \quad \text{Eq. (21)}$$

and to validate in practice, which is one main advantage of set-membership approaches over statistic approaches.

Analog to Eq. (23) and (24), the a-priori and a-posteriori zonotope estimation are given as:

$$\begin{aligned} \langle \mathbf{c}_{\mathbf{e}_k}^-, \mathcal{E}_k^- \rangle &= (\mathbf{F}_{k-1} \odot \langle \mathbf{c}_{\mathbf{e}_{k-1}}^+, \mathcal{E}_{k-1}^+ \rangle) \oplus (\mathbf{G}_{k-1} \odot \langle \mathbf{0}, \mathcal{W}_{k-1} \rangle), \\ \langle \mathbf{c}_{\mathbf{e}_k}^+, \mathcal{E}_k^+ \rangle &= ((\mathbf{I} - \mathbf{K}_k \mathbf{H}_k) \odot \langle \mathbf{c}_{\mathbf{e}_k}^-, \mathcal{E}_k^- \rangle) \oplus (\mathbf{K}_k \odot \langle \mathbf{0}, \mathcal{V}_k \rangle), \end{aligned} \quad (26)$$

where $\mathbf{c}_{\mathbf{e}_k}^-$, \mathcal{E}_k^- , $\mathbf{c}_{\mathbf{e}_k}^+$, \mathcal{E}_k^+ are the center and generation matrix of the a-priori and a-posteriori estimated bounding zonotope for state estimation error \mathbf{e}_k . Since $\langle \mathbf{c}_{\mathbf{e}_k}^-, \mathcal{E}_k^- \rangle$ and $\langle \mathbf{c}_{\mathbf{e}_k}^+, \mathcal{E}_k^+ \rangle$ are iteratively updated using zero-mean zonotopes $\langle \mathbf{0}, \mathcal{E}_0 \rangle$, $\langle \mathbf{0}, \mathcal{W}_k \rangle$, $\langle \mathbf{0}, \mathcal{V}_k \rangle$, the center of the resulting zonotope $\mathbf{c}_{\mathbf{e}_k}^-$ and $\mathbf{c}_{\mathbf{e}_k}^+$ shall be zero, which means

$$\mathbf{e}_k \in \langle \mathbf{0}, \mathcal{E}_k \rangle, \forall k \in \{1, \dots, N\}. \quad (27)$$

Therefore, only the estimation of the generation matrix \mathcal{E}_k^- , \mathcal{E}_k^+ is necessary. Applying Property 1.1. and 1.2. in Eq. (26) results in the zonotope propagation and update as follows:

$$\mathcal{E}_k^- = \mathcal{R}([\mathbf{F}_{k-1} \mathcal{E}_{k-1}^+ \mathbf{G}_{k-1} \mathcal{W}]), \quad (28)$$

$$\mathcal{E}_k^+ = \mathcal{R}([(I - \mathbf{K}_k \mathbf{H}_k) \mathcal{E}_k^- \mathbf{K}_k \mathcal{V}]). \quad (29)$$

The zonotope reduction (denoted as ' \mathcal{R} ' in Eq. (28) and Eq. (29)) is carried out by each zonotope estimation. Without applying zonotope reduction, the dimension of the generation matrices \mathcal{E}_k^- and \mathcal{E}_k^+ increases without limit along the operation time, which is not affordable for computation unit. Further, the error bound $[\mathbf{e}_k]$ of the state estimation can be obtained by applying Eq.(21) on Eq. (28) and Eq. (29).

The integration of the zonotope into the filter structure is summarized as Alg. 1. It should be noted that, Alg. 1 is a general expression, which does not require the applied filter to be EHF. Any other form of the filter, e.g. EKF or

unscented Kalman filter (UKF), could be applied, as long as its error dynamic is known. Applying another filter requires adjusting Eq. (23), (24), (28) and (29) according to the filter dynamic.

E. Vehicle Dynamic Model aided IMU Fault Detection

To accomplish the integrity monitoring of the navigation system, the IMU measurement faults shall be detected, which is achieved by checking the consistency of the IMU measurement with the vehicle dynamic model output. The vehicle used in the current work is an experimental land vehicle equipped with DC motor. However, the proposed FD approach is not limited to this vehicle type. As long as the vehicle, e.g. land vehicles, airplanes or vessels, is equipped with a digital control system and whose dynamic can be grossly modeled, the proposed approach shall be suitable.

It should be mentioned that the dynamic model can also be used as the process model in observers [22]. However, the accuracy of the dynamic model based state estimation depends on numerous factors, e.g. friction factor of the road surface, the operation temperature or wind speed. Therefore, using the dynamic model in state estimation might be a sub-optimal choice, when an industrial class IMU is available for state propagation. In the current work, the dynamic model is only used to generate the threshold of vehicle kinematic, such that the high accuracy of dynamic model is neither critical nor required.

Vehicle Dynamic Model: The vehicle dynamic is modeled as a single track model [23] and the dependency among external forces and vehicle states is summarized as:

$$\dot{\varphi}_D = v_D \cdot \tan \delta / L, \quad (30)$$

$$a_D = F(v_D, I)/m, \quad (31)$$

where 'D' donates the dynamic model relevant variables. v_D and a_D is the velocity and acceleration of the vehicle rear wheel respectively, $\dot{\varphi}_D$ is the heading rate, δ is the steering angle, and L is the vehicle length. Parameter m is the sum of vehicle mass and angular mass. The sum of the external forces F is calculated as a function of the input current I for an electric motor and the speed v_D . The concrete calculation is given in [23]. The current I of DC motor and steering angle δ of the vehicle are control signals, and therefore, known. Further, the rear wheel velocity of the vehicle v_D is measured by an odometer.

Threshold Generation: Given the corresponding standard deviations of the current σ_I , the steering angle σ_δ and the measured absolute velocity σ_v , the intervals of these inputs $[I]$ and $[\delta]$ can be calculated as follows:

$$[I] = [I - n_{\sigma,D} \sigma_I, I + n_{\sigma,D} \sigma_I], \quad (32)$$

$$[\delta] = [\delta - n_{\sigma,D} \sigma_\delta, \delta + n_{\sigma,D} \sigma_\delta], \quad (33)$$

$$[v_D] = [v_D - n_{\sigma,D} \sigma_v, v_D + n_{\sigma,D} \sigma_v], \quad (34)$$

where $n_{\sigma,D}$ denotes sigma-index for interval and presents the confidence level according to the 68–95–99.7 rule in statistic. The threshold generation using the dynamic model should utilize a higher confidence level than the interval

generation of navigation filter, guaranteeing a more robust fault detection.

Based on Eq.(30), Eq.(31) and the prerequisite knowledge of interval arithmetic in [12], the aided intervals of vehicle acceleration $[a_D]$ and rotational rate $[\dot{\varphi}_D]$ can be calculated as follows:

$$[a_D] = F([v_D], [I])/m, \quad (35)$$

$$[\dot{\varphi}_D] = [v_D] \cdot \tan([\delta])/L. \quad (36)$$

Note that the operations 'F', '/', '.' and 'tan' in Eq. (35) and (36) are interval operations, introduced in [12], instead of algebraic operations.

Fault Detection: The specific force in x-direction $f_{ib,x}^b$ and angular rate in z-direction $w_{ib,z}^b$ are calculated from the IMU measurements $\tilde{f}_{ib,x}^b$ and $\tilde{w}_{ib,z}^b$ and their estimated bias $b_{a,x}$ and $b_{g,z}$ [1]:

$$f_{ib,x}^b \approx \tilde{f}_{ib,x}^b - b_{a,x}, \quad (37)$$

$$w_{ib,z}^b \approx \tilde{w}_{ib,z}^b - b_{g,z}. \quad (38)$$

Regarding $f_{ib,x}^b$ as the x-direction acceleration estimated using IMU, it shall not beyond the confidential interval of the vehicle acceleration $[a_D]$ calculated in Eq.(35). Analogically, $w_{ib,z}^b$ shall not beyond $[\dot{\varphi}_D]$ calculated in Eq. (36). An IMU fault will be indicted, if any of $f_{ib,x}^b$ and $w_{ib,z}^b$ is beyond the corresponding threshold. Once the IMU fault is declared, the estimated navigation solution from the main filter is abandoned and switched to the fallback filter, which does not utilize IMU measurements.

III. EXPERIMENTAL EVALUATION

A. Experimental Setup

The designed approach is validated using the data recorded on the experimental platform called 'IRT-Buggy', which is described in [15] in detail. IRT-Buggy is chosen in this paper, due to its digitization, equipped sensors, availability of control signals and dynamic model, and flexibility to be extended with other sensors. Fig.4 shows the measurement setup and sensor distribution on IRT-Buggy, which is used for the real-time data recording. The sensor data is recorded on a 900 MHz single-core rapid control prototyping (RCP) unit, called MicroAutobox II from the manufacturer dSPACE. For inertial

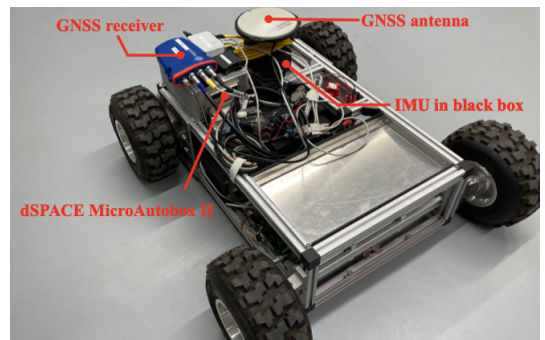


Fig. 4. Photo of the measurement setup equipped on IRT-Buggy

measurements, the setup uses a LORD MicroStrain 3DM®-GX5-25 industrial-class IMU-sensor that is connected via the serial interface, which provides accelerations, angular rates and magnetometer measurements at a rate of 100 Hz.

A Septentrio AstRx3 HDC receiver provides the GNSS observables at a rate of 10 Hz. The communication between the receiver and the RCP unit is achieved via the serial interface. The receiver provides a pulse per second (PPS) signal. Using the PPS, the communication and processing delays of the receiver are measured and compensated [1]. The GNSS correction data is accessed from SAPOS® NRW server as Radio Technical Commission for Maritime Services (RTCM) format by a Raspberry Pi 4, and decoded and recorded in the Raspberry Pi. As the reference for the navigation solution, RTK solution calculated by the Septentrio receiver is used.

The input current of the DC motor, the steering angle and the velocity measurements of IRT-Buggy are provided by the vehicle integrated sensors, which are introduced in [15]. The sensor data is collected by the main-board from IRT-Buggy and transmitted to RCP unit as User Datagram Protocol (UDP) packet via the Ethernet.

Further, the level arm of the antenna position in IMU body-frame \mathbf{L}_A^b is measured as:

$$\mathbf{L}_A^b = (0 \ 0 \ -0.1131 \text{ m})^T. \quad (39)$$

B. Parameterization

Main and Fallback Filter: The initial estimation error covariance matrix of main filter \mathbf{P}_0 is calculated by the initial standard deviation σ_0 given in Tab.I. In fallback filter, the initial standard deviation $\sigma_{0,f}$ contains only the position, velocity, receiver clock bias and drift terms.

TABLE I

INITIAL STANDARD DEVIATIONS OF MAIN FILTER STATES

state	pos. e/n	pos. d	velocity	orientation
σ_0	0.1 m	0.2 m	1 m/s	5 °
state	acc. bias	gyro. bias	clock drift	clock bias
σ_0	0.1 m/s ²	0.01 °/s ²	10 m	10 m/s

For the parameterization of process noise variance matrix \mathbf{Q} , Allan Variance analysis is carried out on applied IMU, estimating accelerometer, gyroscope and their bias process, introduced in [24]. In the fallback filter, an uniform velocity model is applied as process model, assuming the acceleration and rotation of the vehicle is zero. Therefore, the process noise is chosen as noise of the acceleration $\sigma_a = (0.3 \text{ m/s}^2, 0.3 \text{ m/s}^2, 0.1 \text{ m/s}^2)^T$.

The parameterization of measurement noise variance matrix \mathbf{R} for all GNSS observables regarding ν_ρ and ν_d uses sigma- ϵ model, which is sufficient discussed in [1] [24]. The calculation of the standard deviation is given as:

$$\sigma_\rho^2 = C_\rho^2 \cdot 10^{-\frac{C/N_0}{10}}, \quad \sigma_d^2 = C_d^2 \cdot 10^{-\frac{C/N_0}{10}}, \quad (40)$$

where C/N_0 is the carrier-to-noise ration in dB/Hz and provided by the GNSS receiver. C_ρ and C_d are tuning parameter defined for pseudorange and deltarange measurements,

separately. In current work, the optimal choice of C_ρ and C_d is considered as 60 m and 2 m/s, regarding the used GNSS correction method: GPS L1 differential correction. This results in a range of standard deviation for pseudorange measurements ca. $0.5 \sim 2 \text{ m}$ and for deltarange measurement $0.1 \sim 0.7 \text{ m/s}$.

Zonotope: The reduction parameter q of zonotope discussed in Sec.II-C is set to 4000, considering the balance between the overestimation and computational load. A discussion of the choice of q is given in Sec. III-E. Besides, $n_{\sigma,z}$ is set to 3 for zonotope estimation. Particularly, the 3D position term of \mathcal{E}_0 is initialized as $(10 \text{ m}, 10 \text{ m}, 20 \text{ m})^T$ for PL robustness.

Vehicle Dynamic Model: To strengthen the confidence of the vehicle dynamic model discussed in Sec.II-E and guarantee a more robust fault detection, the threshold is generated with a higher confidence level: $n_{\sigma,D} = 6$. By analyzing the historical measurement data from the IRT-Buggy, the standard deviation of the odometer velocity measurements σ_v , of the current of DC motor σ_I and the steering angle σ_δ are set as 0.1 m/s, 1 A and 1 °, respectively.

C. Experiment Overview

In this subsection, the test scenario of the experimental evaluation is described, followed with an overview of the designed experiments. The first subfigure in Fig.5 shows the bird eye view of the RTK reference trajectory in a local NED-frame, whose origin is the start point of the vehicle. The drive is carried out in open area without GNSS signal shadowing or disturbance, because GNSS integrity is no major concern of the current publication. The second subfigure shows the reference velocity of the vehicle. Combining both subfigures, it can be observed that the vehicles drives firstly 2 rounds of large circle from 35 to 130 seconds. Then it drives repeatedly small circles in the middle from 200 seconds to 350 seconds.

The experimental evaluation is divided into three parts:

- comparison between EHF and EKF, regarding the positioning accuracy under optimal or inappropriate param-

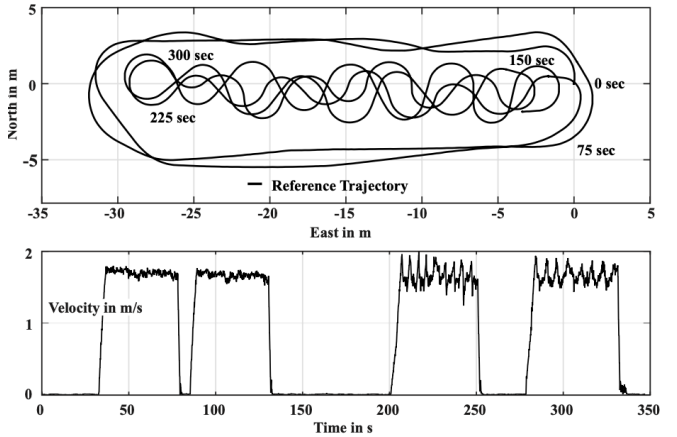


Fig. 5. Bird eye view of the RTK reference driven trajectory and reference velocity of the vehicle

TABLE II
ACCURACY INDICATORS OF 2D AND 3D ERROR OF FILTERS NAVIGATION SOLUTION UNDER DIFFERENT SETTINGS

Setting	2D Error of EKF [m]				2D Error of EHF [m]				3D Error of EKF [m]				3D Error of EHF [m]			
	Mean	Sigma	RMS	95%												
01	0.231	0.107	0.254	0.437	0.232	0.118	0.260	0.469	0.503	0.192	0.538	0.808	0.454	0.224	0.507	0.875
02	0.388	0.335	0.513	1.101	0.233	0.118	0.261	0.473	0.593	0.385	0.707	1.289	0.458	0.224	0.510	0.870
03	divergent				0.232	0.119	0.261	0.429	divergent				0.492	0.292	0.572	0.977
04	0.238	0.140	0.276	0.557	0.226	0.132	0.262	0.515	0.641	0.322	0.717	1.100	0.490	0.268	0.559	0.914
05	divergent				0.242	0.130	0.275	0.497	divergent				0.459	0.233	0.514	0.849
06	0.616	6.463	6.492	0.921	0.198	0.126	0.235	0.456	0.821	6.459	6.511	0.996	0.402	0.199	0.449	0.750
07	0.421	0.319	0.529	1.196	0.238	0.121	0.267	0.480	1.098	0.592	1.247	2.206	0.467	0.243	0.527	0.904

eter setting or with artificial initialization error.

- validation of PL generation using zonotope
- validation of FD and fallback filter against real-world and artificial vibration fault of IMU

D. Comparison between EHF and EKF

The comparison is conducted in seven test scenarios under various initialization conditions or parameter settings:

01. default parameters given in Sec.III-B: P_0 , Q and R , and without artificial initialization error;
02. Setting 01 with artificial initialization error: 30° added on yaw angle;
03. Setting 01 with artificial initialization error: 60° added on yaw angle;
04. Setting 01 with falsified parameter for pseudorange and deltarange variance: $C_p = 180$ m, $C_d = 6$ m/s;
05. Setting 01 with falsified parameter for pseudorange and deltarange variance: $C_p = 30$ m, $C_d = 1$ m/s;
06. Setting 01 with falsified parameter for initial standard deviation of position: $(0.02$ m, 0.02 m, 0.05 m) T ;
07. Setting 01 with falsified parameter for initial standard deviation of position: $(1$ m, 1 m, 2 m) T .

Fig.6 shows the 2D and 3D error of EHF and EKF estimation during the drive under Setting 01. The first subfigure shows that with the default parameters, EHF does not show much advantage against EKF. This indicates that estimation accuracy under ideal operation condition is no

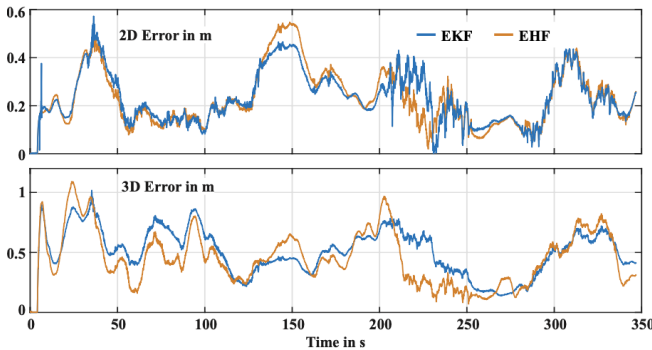


Fig. 6. 2D and 3D error of filters EKF and EHF under Setting 01

major strength of EHF. Meanwhile, the 3D error comparison indicates a slightly more accurate estimation in the vertical direction from EHF than EKF. In general, the error in vertical direction is ca. twice as the one in horizontal direction. The reason is given in [25] (pp. 328-332): in average, the positioning error in vertical direction is 1.6 times such high as the one in horizontal direction with the same GNSS measurements. This is a result of the satellite-constellation limitation: satellites distribute only above the horizon, and therefore, are not evenly distributed in vertical direction. This result proves the robustness and advantage of EHF against non-optimal operation condition.

Besides, Tab. II presents various quality indicators of the 2D and 3D accuracy, including the average ('Mean'), the standard deviation ('Sigma'), 95% accuracy ('95%') and rooted mean square (RMS) of the positioning error. In Tab. II, Setting 01 shall be regarded as a reference performance for evaluating other settings.

With artificial initialization error (Setting 02 and 03), the downgrade of all indicators of EKF is notable, EKF is even divergent under Setting 03, while the EHF maintains the same accuracy level as Setting 01. This validates a better robustness of EHF against initialization error. It should be mentioned that the artificial error is chosen to be added on initial yaw angle, because the yaw angle is commonly initialized with magnetometer measurement from the IMU. When the IMU is not properly calibrated in the operation place, such orientation error might occur, due to electromagnetic fields generated by motors or electromagnetic shielding caused by iron equipment near the IMU.

With falsified parameterization (Setting 04, 05, 06 and 07), the results indicates even more advantage of EHF over EKF. It can be obtained that setting the measurement variance too wide (Setting 04) slightly increases the 3D error of EKF, while setting it too narrow (Setting 05) makes EKF divergent. Again, the EHF maintains the same accuracy level as Setting 01, which proves the robustness of EHF against inappropriate measurement parameterization. Setting 04 and 05 are chosen, because parameterization of GNSS measurements is difficult to evaluate and validate in real-time applications. Therefore, the robustness of the applied filter against inappropriate measurement parameterization is

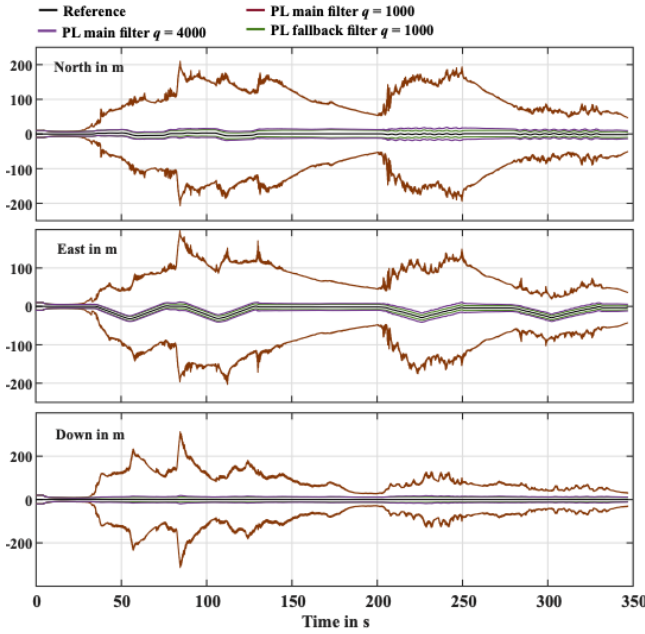


Fig. 7. Validation of PL generation with reduction order: reference position and calculated error bound by the main and fallback filter under various q

extremely crucial. Further, the robustness of EHF against false parameterization of initial state variance is also notable with Setting 06 and 07.

In conclusion, the experiment results indicates enormous advantage of EHF over EKF, regarding common abbreviations by utilizing GNSS aided INS, i.e. poor initialization and inappropriate parameterization.

E. Validation of PL Generation using Zonotope

The core issue of PL calculation is to bound the state estimation error, which means the true states (in practice the reference states) must be wrapped by the calculated upper and lower bound. Fig. 7 shows that the generated PL is capable of wrapping the reference during the whole drive, which validates the correctness of PL generation by the main and fallback filter under various reduction order q . Comparing the generated PL by the main filter under $q = 1000$ and $q = 4000$, the overestimation effect with

reduction order $q = 1000$ is notable: the generated PL coincides with the dynamic only in the minority of the driving time, which indicates that the overestimation effect of the zonotope estimation dominates the PL generation mostly. Meanwhile, the overestimation is not observable for the fallback filter even by $q = 1000$, due to its lower system order, and therefore, much lower computation complexity. In the main filter, the state vector \mathbf{x} contains 18 states, including the quaternion $\mathbf{q}_b^n \in \mathbb{R}^{4 \times 1}$. By the estimation of state error covariance \mathbf{P} , the error of orientation vector is considered [20], which makes $\mathbf{P} \in \mathbb{R}^{17 \times 17}$. Therefore, the error space of the main filter is 17-dimensional, while the one of the fallback filter is 8-dimensional. This results in the generation matrix for the main filter $\mathcal{E} \in \mathbb{R}^{17 \times q}$ and for the fallback filter $\mathcal{E}_f \in \mathbb{R}^{8 \times q}$.

Further, Tab. III shows the average width of estimated PL using various reduction order q within the main filter. The post-processing is carried out using MATLAB & Simulink platform on a Laptop, which is equipped with an Intel® Core(TM) i7-7700HQ CPU @ 2.80GHz. Therefore, the run time evaluation can only be regarded as an evaluation of computational load, rather than a validation of real-time capability, because no real-time hardware is applied for the computation. During the simulation, only single core of the CPU is utilized. The run time given in Tab. III contains only the computation time of zonotope, the computation time of other components within the navigation system is not included.

As discussed in Sec. II-C, the smaller q indicates larger overestimation of the zonotope and smaller computational load. With increasing reduction order, the width of the estimated PL decreases. However, from $q = 8000$ to $q = 16000$, the decrease of PL is not significant. Considering the balance of computational load and degree of zonotope overestimation, the reduction order of between $q = 4000$ and $q = 8000$ is suggested for the current navigation system for real-time application.

F. Validation of FD and Fallback Filter

Fig.8 depicts the acceleration in x-direction and rotational rate in z-direction measured by the IMU, together with their corresponding thresholds generated by vehicle dynamic model, respectively. It shall be mentioned that, the acceleration and rotational rate of IMU considers the estimated bias from the main filter, as explained in Eq. (37) and (38).

In the first subfigure, the notable noise (up to $\pm 2 \text{ m/s}^2$) on the IMU accelerometer measurement can be observed, which mainly comes from the vibration of IRT-Buggy. By design of the IRT-Buggy, the high frequency vibration from the DC motor and its influence on the inertial sensor were not sufficient considered. Therefore, no sufficient vibration damping is designed for industrial IMU. Observing the recorded IMU accelerometer measurements, the description in [26] is verified, that IMU accelerometer is sensitive to vibration and IMU measurements could, therefore, be seriously disturbed by massive measurement noise.

TABLE III

MEAN OF GENERATED PL USING ZONOTOPE AND COMPUTATION TIME WITH VARIOUS REDUCTION PARAMETER q

q		1000	2000	4000	8000	16000
PL north in m	main filter	97.015	17.079	12.450	8.744	8.022
	fallback filter	8.928	8.419	7.830	7.478	7.377
PL east in m	main filter	80.343	12.840	9.213	6.766	6.299
	fallback filter	6.233	6.014	5.757	5.594	5.534
PL down in m	main filter	81.410	17.425	13.418	10.570	9.931
	fallback filter	11.312	10.745	10.183	9.847	9.726
Run time in s	main filter	52.55	88.85	182.49	348.25	755.41
	fallback filter	20.40	39.15	81.22	213.11	372.43

Regarding the validation of IMU fault detection, the noisy IMU measurement exceeds its threshold at multiple moments, indicating IMU fault. To verify the fault indication, a low-pass filter is introduced to suppress the notable measurements noise of IMU accelerometer. After filtering, it can be observed that the dynamic of the IMU acceleration coincides with that of threshold approximately, and the filtered measurement is within the threshold for the majority of the validation time. Thus, the generated acceleration threshold and FD are valid.

In the second subfigure of Fig.8, the rotational rate measured by IMU has the same trend as the generated threshold and lies within the threshold. Thus, there is no fault alarm in terms of angular rate. Combining both subfigures in Fig.8, it can be concluded that the vehicle dynamic model aided acceleration and angular rate threshold generation and the FD of real-world IMU vibration fault are valid.

Fig. 9 shows the 2D and 3D error of the position estimation under following settings:

- EKF;
- EHF stand alone, which refers to EHF without FD and fallback option;
- the entire designed approach, which refers to the scheme illustrated in Fig. 1.

In Fig. 9, gray zone marks the period, when additional artificial measurement noise is added on IMU measurements with standard deviation of 10 m/s^2 , simulating a stronger vibration of the vehicle. From the beginning to 200 seconds, the IMU measurements with real-world vibrations described in Fig. 8, are utilized. Surprisingly, neither EKF nor EHF is disturbed by this scale of measurement noise. The reason is that the high accurate pseudorange and deltarange measurements are fed to the filter at 10 Hz, such that the high-accurate measurement update dominated the state estimation accuracy. However, the long-term stability of filtering with such unexpected noise behavior of inertial sensor measurement, remains to be studied.

After excessive noise is added on the measurement, a rapid increase of the 3D estimation error from EKF can be observed, up to 6 m. Meanwhile, the accuracy of EHF does not downgrade a lot, which proves the robustness of EHF against

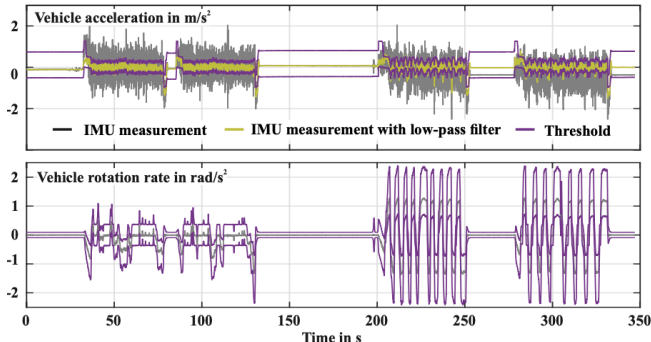


Fig. 8. Acceleration in x-direction and rotational rate in z-direction, together with their threshold

non-optimal operation condition, again. Further, the entire designed approach shows better 2D and 3D accuracy than EHF stand alone after 200 seconds. This proves the necessity of the fallback option, which maintains the usability of the navigation system, when the excessive measurement fault is detected by the integrity system.

IV. CONCLUSION

This publication presented a novel scheme for robust state estimation and integrity monitoring within a tightly-coupled navigation system, involving EHF, zonotope and vehicle dynamic model aided INS fault detection.

Applying EHF aims at robust state estimation under unsatisfactory operation condition or system disturbances. This was first explained theoretically, and then validated in the post-processing environment with recorded data. The experimental results show tremendous robustness of EHF against poor initialization, false parameterization and undesired excessive measurement noise from inertial sensor. Considering the difficulty of the appropriate parametrization by applying EKF in GNSS aided INS, EHF is suggested to be an ideal alternative to EKF, except that the computation capacity is extremely limited for an LMI solver, e.g. for microcontroller or comparable computation unit. Especially for automotive applications, applying EHF might have greater advantages, where the quality of GNSS measurement varies continuously due to ever-changing operation environment. In such application, an unitary parametrization strategy might not satisfy the accuracy requirement using conventional EKF.

Further, a feasibility studied was carried out for applying zonotope in a tightly-coupled navigation system for PL generation, which is a high-order non-linear system. The experimental results prove that applying zonotope for PL generation is valid. However, this method is computational intensive when a large reduction order q is required, due to high system complexity. Regarding the experimental results, zonotope is considered suitable for 3-degree of freedom (DOF) system (the fallback filter in the current publication). An example shall be automotive application, where the vehicle orientation is roughly considered as the velocity direction. For a 6-DOF (the main filter in the current publi-

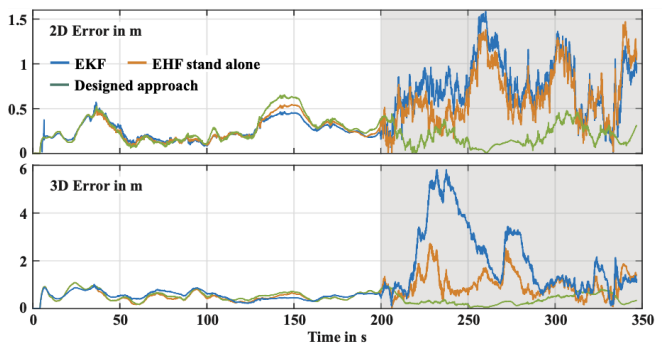


Fig. 9. 2D and 3D error of the position estimation from EKF, EHF stand alone and the entire designed approach, the gray zone marked the period with additional artificial vibration fault

cation), applying zonotope is still feasible, when a powerful computational unit is available.

Finally, a vehicle dynamic model aided FD of inertial sensor was introduced and evaluated. The experimental results verify the correctness of FD and indicates that applying a fallback option improves the accuracy of state estimation under serious IMU measurement faults. This approach is suitable for vehicles equipped with digital control systems. Normally in such systems, the vehicle dynamic is modeled and used in control systems, and therefore, the control signal and corresponding dynamic model are available. Meanwhile, the kinematic model is used for process model by utilizing an inertial sensor. In such systems, a consistency check to realize FD of inertial sensor is simple to achieve and valid.

In future works, a real-time implementation and application of the designed approach is aimed. Especially, the real-time evaluation and validation are desired, which operates on vehicles with higher dynamic and under more real-world disturbances. Further, it would be great research interests of the authors, to extended the proposed approach on the control system, to accomplish a reliable guidance, navigation and control (GNC) system for safety-critical applications.

REFERENCES

- [1] T. Konrad, J.-J. Gehrt, J. Lin, R. Zweigel, and D. Abel, "Advanced state estimation for navigation of automated vehicles," *Annual Reviews in Control*, vol. 46, pp. 181–195, 2018.
- [2] U. I. Bhatti and W. Y. Ochieng, "Failure Modes and Models for Integrated GPS/INS Systems," *Journal of Navigation*, vol. 60, no. 2, pp. 327–348, 2007.
- [3] P. D. Groves, *Principles of GNSS, inertial, and multisensor integrated navigation systems*, second edition ed., ser. GNSS technology and application series. Boston: Artech house, 2013.
- [4] D. Simon, *Optimal State Estimation: Kalman, H Infinity, and Nonlinear Approaches*. John Wiley & Sons, Inc, 2006.
- [5] S. Liu, J.-J. Gehrt, D. Abel, and R. Zweigel, "Dual-Constellation Aided High Integrity and High Accuracy Navigation Filter for Maritime Applications," in *Proceedings of the 2019 International Technical Meeting (ITM 2019) of The Institute of Navigation*, 2019, pp. 762–774.
- [6] S. Liu, J. Gehrt, D. Abel, and R. Zweigel, "Identification of multi-faults in gnss signals using rsivia under dual constellation," *Acta Cybernetica*, 2020.
- [7] Z. Maiying, G. Jia, G. Dingfei, and Y. Zhaohua, "An extended h_1/h_∞ optimization approach to fault detection of ins/gps-integrated system," *IEEE Transactions on Instrumentation and Measurement*, vol. 65, no. 11, pp. 2495–2504, 2016.
- [8] H. Rafaralahy, E. Richard, M. Boutayeb, and M. Zasadzinski, "Simultaneous observer based sensor diagnosis and speed estimation of unmanned aerial vehicle," in *Proceedings of the 31st International Technical Meeting of the Satellite Division of The Institute of Navigation (ION GNSS+ 2018)*, 2018, pp. 2440 – 2455.
- [9] J. Lee, M. Kim, and S. Pullen, "Integrity assurance of kalman-filter based gnss/imu integrated systems against imu faults for uav applications," in *the 31st International Technical Meeting of the Satellite Division of the Institute of Navigation*, 2018, p. 2484–2500.
- [10] C. Combaste, "A state bounding observer based on zonotopes," in *European Control Conference*, 2003, pp. 2589–2594.
- [11] C. Combaste, "A state bounding observer for uncertain non-linear continuous-time systems based on zonotopes," in *Proceedings of the 44th IEEE Conference on Decision and Control, and the European Control Conference 2005*, 2005, pp. 7228–7234.
- [12] R. Moore, R. Kearfott, and M. Cloud, *Introduction to Interval Analysis*. Society for Industrial and Applied Mathematics (SIAM), 2009.
- [13] W. Kühn, "Rigorously computed orbits of dynamical systems without the wrapping effect," *Computing*, vol. 61, no. 6, pp. 47–67, 1998.
- [14] W. Zhang, Z. Wang, T. Raïssi, Y. Wang, and Y. Shen, "A state augmentation approach to interval fault estimation for descriptor systems," *European Journal of Control*, vol. 51, pp. 19–29, 2020.
- [15] M. Reiter, M. Wehr, F. Sehr, A. Trzuskowsky, R. Taborsky, and D. Abel, "The IRT-Buggy – Vehicle Platform for Research and Education," *IFAC-PapersOnLine*, vol. 50, no. 1, pp. 12 588–12 595, 2017.
- [16] M. Osman, R. Alonso, A. Hammam, F. M. Moreno, A. Al-Kaff, and A. Hussein, "Multisensor fusion localization using extended h_∞ filter using pre-filtered sensors measurements," in *2019 IEEE Intelligent Vehicles Symposium (IV)*, 2019, pp. 1139–1144.
- [17] J. Y. Loo, C. P. Tan, and S. G. Nurzaman, "H-infinity based extended kalman filter for state estimation in highly non-linear soft robotic system," in *2019 American Control Conference (ACC)*, 2019, pp. 5154–5160.
- [18] B. Hassibi and A. Sayed, "Linear estimation in krein spaces- prat ii: Applications," *IEEE Transaction on Automatic Control*, vol. 41, no. 1, pp. 34–49, 1996.
- [19] J.-J. Gehrt, R. Zweigel, T. Konrad, and D. Abel, "DVL-aided Navigation Filter for Maritime Applications," *IFAC-PapersOnLine*, vol. 51, no. 29, pp. 418–423, 2018.
- [20] J. Wendel, *Integrierte Navigationssysteme: Sensordatenfusion, GPS und Inertiale Navigation*, ser. Naturwissenschaft und Technik 1/2010. München: Oldenbourg Wissenschaftsverlag, 2009.
- [21] C. Combastel, "An extended zonotopic and gaussian kalman filter (ezgkf) merging set-membership and stochastic paradigms: Toward non-linear filtering and fault detection," *Annual Reviews in Control*, vol. 42, pp. 232–243, 2016.
- [22] D. C. Salmon and D. M. Bevly, "An exploration of low-cost sensor and vehicle model solutions for ground vehicle navigation," in *2014 IEEE/ION Position, Location and Navigation Symposium - PLANS 2014*, 2014, pp. 462–471.
- [23] S. Liu, S. Roy, E. Pairet-Garcia, J.-J. Gehrt, F. Siemer, C. Büskens, D. Abel, and R. Zweigel, "Case study: Networked control for optimal maneuvering of autonomous vessels," *IFAC PapersOnLine*, vol. 52, no. 8, p. 440–445, 2019.
- [24] M. Breuer, T. Konrad, and D. Abel, "High precision localisation in customised gnss receiver for railway applications," in *Proceedings of the 29th International Technical Meeting of The Satellite Division of the Institute of Navigation (ION GNSS+ 2016)*, 2016, pp. 779–787.
- [25] E. Kaplan and C. Hegarty, *Understanding GPS Principles and Applications: Principles and Applications*, 2nd ed. Norwood: Artech house, 2005.
- [26] D. Tomaszewski and M. Smieja, "Analysis of the use of integrated imu module for vibration measurements," in *Proceedings of the International Conference on Environmental Engineering*, 2014, p. 2029–7092.